

Variational Autoregressive Networks Applied to ϕ^4 Field Theory Systems

Moxian Qian^a Shiyang Chen^b

^a*School of Science and Engineering, The Chinese University of Hong Kong, Shenzhen (CUHK-Shenzhen), Guangdong, 518172, China*

^b*Department of Physics, Swansea University, SA2 8PP, Swansea, United Kingdom*

E-mail: qianmoxian@cuhk.edu.cn, chenshiyang@swansea.edu.cn

ABSTRACT: We combine reinforcement learning with variational autoregressive networks (VANs) to perform data-free training and sampling for the discrete Ising model and the continuous ϕ^4 scalar field theory. We quantify the complexity of the target distribution via the KL divergence between the magnetization distribution and a reference Gaussian distribution, and observe that configurations with smaller KL divergence typically require fewer training steps. Motivated by this observation, we investigate transfer learning and show that fine-tuning models pretrained at a single value of κ can reduce training time compared with training from a Gaussian field. In addition, inspired by single-site and cluster Monte Carlo updates, we introduce single-site and block Metropolis–Hastings (MH) updates on top of VAN proposals. These MH corrections systematically reduce the residual bias of pure VAN sampling in the parameter range we study, while maintaining high sampling efficiency in terms of the effective sample size (ESS). For both the Ising model and the ϕ^4 theory, our results agree with standard Monte Carlo benchmarks within errors, and no clear critical slowing down is observed in the explored parameter ranges.

KEYWORDS: Algorithms and Theoretical Developments, Lattice Quantum Field Theory, Non-Perturbative Renormalization

Contents

1	Introduction	2
2	Method	3
2.1	Model definitions	3
2.1.1	Two-dimensional Ising model	3
2.1.2	Two-dimensional ϕ^4 scalar field theory	3
2.2	Autoregressive sampling framework	3
2.2.1	Discrete system: Ising model	4
2.2.2	Continuous system: ϕ^4 theory	5
2.3	Effective sample size	5
2.4	Metropolis–Hastings correction strategies	6
2.5	Training and benchmark methods	8
3	Discrete system: Ising model results	8
3.1	Thermodynamic observables	8
3.2	Effective sample size analysis	9
4	Continuous system: ϕ^4 theory results	9
5	Transfer learning	11
5.1	Transfer learning strategies	11
5.2	Transfer across coupling parameters	11
5.3	Transfer across lattice sizes	13
5.4	KL divergence and training complexity	14
6	Conclusion	16
7	Acknowledgments	17
A	Network architecture	19
B	Training algorithms	20
C	Detailed comparison between generative models and MC algorithms	20
C.1	Overview table	21
C.2	Block updates	21
C.3	Diffusion models, Langevin dynamics, and stochastic quantization	21
C.4	Normalizing flows and flow matching	22
D	Analytical VAN for a two-dimensional Gaussian mixture	22

1 Introduction

Accurate computation of physical observables in lattice field theory and statistical mechanical systems is a fundamental challenge in computational physics. In high dimensions, analytical calculations are usually intractable, and one must resort to numerical sampling methods to extract observables from the discretized partition function. Traditional Monte Carlo (MC) methods can be categorized into local updates (such as the Metropolis–Hastings algorithm) and global updates (such as Wolff cluster algorithms). However, these methods suffer from critical slowing down near critical points or in large lattice systems, where the autocorrelation time diverges with system size or correlation length [1]; in systems such as $U(1)$ gauge fields they may also encounter topological freezing [2], where the topological charge cannot be effectively updated along long Markov chains.

In recent years, generation models from deep learning have been widely applied in attempts to overcome these issues. Normalizing flows [3, 4] and their continuous variants [5] map simple distributions to target distributions via invertible transformations, but such variational training based on the reverse KL divergence often suffers from mode collapse in high-dimensional systems, which is believed to be related to the curse of dimensionality [6]. Another class of methods, including diffusion models [7, 8], flow matching [9] and rectified flows [10], employ the forward KL divergence for data-driven training and thus can partially avoid mode collapse. A common feature of these approaches is that they perform global updates and generate an entire field configuration in one shot. Such flow- and diffusion-based approaches have also been successfully applied to lattice field theory and lattice QCD [6, 11–14].

Compared with these global-update methods, autoregressive models [15, 16] factorize the joint distribution using the Bayesian chain rule and generate samples by sequentially predicting conditional probabilities. This is intrinsically similar to single-site update schemes of local Monte Carlo algorithms. One may expect that such local-update characteristics could help avoid some of the difficulties encountered by global methods in high dimensions. Autoregressive methods have already been successfully applied to statistic spin systems such as the Ising xy model model [17, 18], demonstrating favorable sampling efficiency. However, their applicability to continuous field theories has not yet been systematically explored.

In this work, we extend variational autoregressive networks (VANs) from discrete systems to the continuous ϕ^4 scalar field theory. Our main contributions are:

1. We propose an autoregressive sampling framework suitable for continuous fields, combined with single-site Metropolis–Hastings corrections that systematically reduce the residual bias of pure VAN sampling and, in principle, allow one to recover exact Markovian equilibrium with respect to an auxiliary target distribution;
2. Inspired by non-local cluster updates such as the Wolff algorithm, we introduce block MH updates that simultaneously modify multiple lattice sites, improving mixing at fixed MH step count;

3. We systematically investigate transfer learning strategies, use the KL divergence between the magnetization distribution and a Gaussian reference to quantify the complexity of the target distribution, and demonstrate that transfer learning can significantly accelerate training across parameter space and lattice sizes.

Our numerical experiments show that the proposed method can efficiently sample the ϕ^4 theory on lattices up to $L = 10$ and for $\kappa \in [0.20, 0.30]$. Within our statistical precision we do not observe clear critical slowing down.

The rest of the paper is organized as follows. In Sec. 2 we introduce the basic framework of autoregressive models and the reinforcement learning training scheme. Sec. 3 presents metropolis hasting for the Ising model. Sec. 4 discusses sampling results for the ϕ^4 theory in detail, including comparisons of different MH correction strategies. Sec. 5 analyzes the mechanism behind transfer-learning speedup. Sec. 6 concludes.

2 Method

2.1 Model definitions

2.1.1 Two-dimensional Ising model

The ferromagnetic two-dimensional Ising model is defined on an $L \times L$ square lattice with periodic boundary conditions. The Hamiltonian is

$$H(\sigma) = -J \sum_{\langle i,j \rangle} \sigma_i \sigma_j, \quad (2.1)$$

where $\sigma_i = \pm 1$ are Ising spins, $J > 0$ is the ferromagnetic coupling (set to $J = 1$ hereafter), and the sum runs over nearest-neighbour bonds. The model exhibits a second-order phase transition at the critical temperature $T_c/J = 2/\ln(1 + \sqrt{2}) \approx 2.269$ (with $k_B = 1$).

2.1.2 Two-dimensional ϕ^4 scalar field theory

The Euclidean action of two-dimensional ϕ^4 scalar field theory on an $L \times L$ square lattice with periodic boundary conditions reads,

$$S[\phi] = \sum_x \left[-2\kappa \sum_{\mu=1,2} \phi_x \phi_{x+\hat{\mu}} + (1 - 2\lambda) \phi_x^2 + \lambda \phi_x^4 \right], \quad (2.2)$$

where $\phi_x \in \mathbb{R}$ is a continuous field variable, κ is the hopping parameter, and λ is the quartic coupling. In this work, We fix $\lambda = 0.022$, for which the theory has a second-order phase transition at $\kappa_c \approx 0.239$ in the infinite-volume limit $L \rightarrow \infty$.

2.2 Autoregressive sampling framework

Autoregressive models factorize the joint distribution via the chain rule into a product of conditional probabilities:

$$p_{\theta}(\mathbf{s}) = \prod_{i=1}^{L^2} p_{\theta}(s_i | s_{<i}), \quad (2.3)$$

where s_i denotes the degree of freedom at lattice site i and $s_{<i} = \{s_1, \dots, s_{i-1}\}$ denotes all sites preceding i in a predefined ordering. Such site-by-site generation is structurally similar to single-site update sweeps of traditional Monte Carlo methods.

To illustrate this framework, we consider a simple two-dimensional Gaussian mixture as a toy model (the full analytical derivation is given in Appendix D). As shown in Fig. 1, the VAN sampling process converts a unimodal prior into a bimodal target distribution in two sequential steps: first sample s_1 from the marginal distribution $p(s_1)$, then sample s_2 from the conditional distribution $p(s_2|s_1)$. The resulting L-shaped trajectories visualize how samples are routed to different modes according to the posterior weights $w(s_1)$.

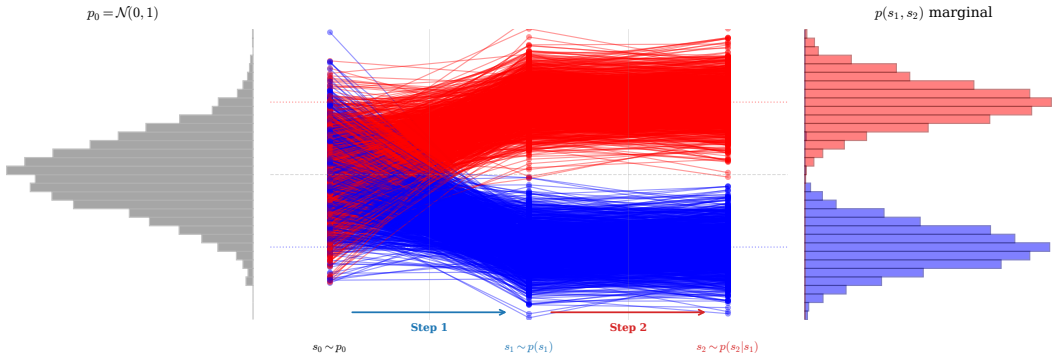


Figure 1: Illustration of the VAN sampling process on a two-dimensional Gaussian mixture. **Left:** prior distribution $p_0 = \mathcal{N}(0, 1)$. **Middle:** sampling trajectories—step 1 draws s_1 from $p(s_1)$ (horizontal moves), step 2 draws s_2 from $p(s_2|s_1)$ (vertical moves). Blue and red trajectories are routed to the left and right modes, respectively. **Right:** the target bimodal distribution $p(s_1, s_2)$.

2.2.1 Discrete system: Ising model

For the Ising model, the conditional distribution is taken to be Bernoulli [17]:

$$p_\theta(\sigma_i = +1 | \sigma_{<i}) = \text{sigmoid}(f_\theta(\sigma_{<i})), \quad (2.4)$$

where f_θ is an autoregressive neural network (such as PixelCNN [15] or MADE [16]). During sampling, for $i = 1, 2, \dots, L^2$, we sequentially draw spin values from the conditional distributions to obtain a complete configuration.

Figure 2 shows the autoregressive sampling process of a VAN on a 3×3 Ising model, demonstrating how the network learns nontrivial patterns in conditional probabilities.

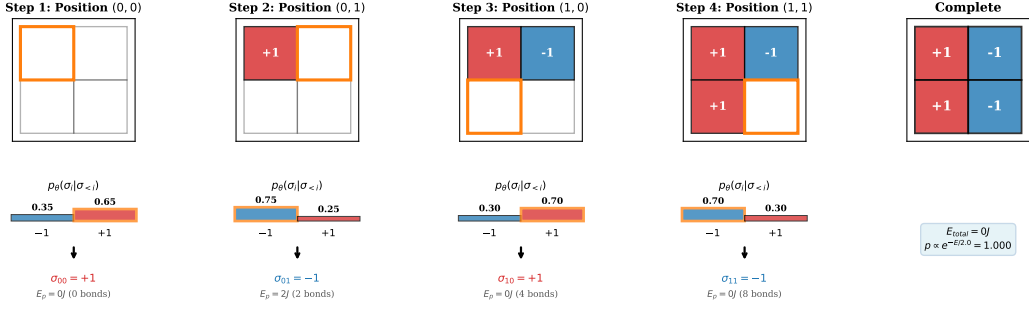


Figure 2: Autoregressive sampling process of a VAN on a 3×3 Ising model. **Top row:** sequential evolution of lattice configurations, with the current sampling site highlighted by an orange frame. **Middle row:** conditional distributions $p_{\theta}(\sigma_i | \sigma_{<i})$ output by the network at each step, with the sampled value highlighted by an orange frame. **Bottom row:** sampling descriptions, showing the conditional formulas, sampled spins, and partial energy contributions. The network learns nontrivial patterns: for example, in step 2, despite ferromagnetic nearest-neighbor couplings, one finds $P(\sigma_{01} = -1 | \sigma_{00} = +1) = 0.75$, reflecting global energy optimization.

2.2.2 Continuous system: ϕ^4 theory

Extending the autoregressive framework to continuous field systems requires an appropriate parameterization of the conditional distributions. In this work we use Gaussian conditionals:

$$p_{\theta}(\phi_i | \phi_{<i}) = \mathcal{N}(\phi_i; \mu_i, \sigma_i^2), \quad (2.5)$$

where the mean μ_i and log-standard deviation $\log \sigma_i$ are outputs of a neural network:

$$(\mu_i, \log \sigma_i) = \text{PixelCNN}_{\theta}(\phi_{<i}). \quad (2.6)$$

The key requirement of this extension is that the network must learn the local means of the field (determined by neighboring field values) and local fluctuations (determined by temperature and coupling parameters). Our architecture consists of 3–6 convolutional layers (64–128 channels) using 7×7 masked convolution kernels and PReLU activations. The output layer has two channels (corresponding to μ and $\log \sigma$). Detailed architectural design is given in Appendix A.

2.3 Effective sample size

In this work, importance-sampling weights is used to monitor sampling efficiency within an autoregressive sampling and Metropolis–Hastings correction framework. Let $\{\mathbf{s}^{(i)}\}_{i=1}^N$ be a set of samples drawn from a proposal distribution $q(\mathbf{s})$ (e.g. p_{θ} or a combination thereof), with respect to a target density $\pi(\mathbf{s})$. The corresponding importance weights are measured by Kish’s formula [6, 12],

$$N_{\text{eff}}^{\text{IS}} = \frac{\left(\sum_{i=1}^N w_i\right)^2}{\sum_{i=1}^N w_i^2}, \quad \text{with,} \quad w_i = \frac{\pi(\mathbf{s}^{(i)})}{q(\mathbf{s}^{(i)})}. \quad (2.7)$$

This metric equals the nominal sample size N as weights are nearly uniform, reflecting efficient sampling. Conversely, if the weight distribution becomes highly uneven—meaning only a small fraction of samples dominate the statistical weight—the denominator grows large and $N_{\text{eff}}^{\text{IS}}$ drops substantially, signaling a loss of effective samples due to weight degeneracy. For convenient comparison of sampling efficiency across parameters and algorithms, we report the normalized effective sample size

$$\text{ESS}_{\text{norm}} \equiv \frac{N_{\text{eff}}^{\text{IS}}}{N} \in (0, 1]. \quad (2.8)$$

Throughout the paper, the term “ESS” in all figures and tables refers to this normalized quantity.

2.4 Metropolis–Hastings correction strategies

Learned distribution generally differs from the exact Boltzmann distribution $p_\beta(\mathbf{s}) \propto e^{-\beta H(\mathbf{s})}$. To ensure the constructed Markov chains converges asymptotically to the our target distribution, we apply Metropolis–Hastings (MH) correction [19] following each autoregressive proposal. This step eliminates the bias introduced by the neural sampler while preserving detailed balance with respect to a target distribution.

In our implementation for the ϕ^4 theory, VANs serves both as a component of transition amplitude,

$$\pi(\mathbf{s}) \propto p_\theta(\mathbf{s}) e^{-\beta H(\mathbf{s})}, \quad (2.9)$$

and perform MH updates to remove residual deviations. When p_θ closely approximates the target distribution, the MH correction typically yields a high acceptance rate. We consider two variants of Metropolis–Hastings correction: single-site updates and block update

Single-site MH correction follows the same conceptual outline as a conventional single-site Metropolis update, except that the learned density p_θ appears in the acceptance probability. The single-site HM update implements symmetric local proposals—spin flips for the Ising model or Gaussian perturbations for the ϕ^4 theory with acceptance decisions based solely on the change. Starting from an initial configuration \mathbf{s} from the VAN, the sequential single-site MH algorithm as described in Algorithm 1.

Algorithm 1 Single-site Metropolis–Hastings correction

Require: VAN-generated configuration \mathbf{s} , number of MH steps N_{MH}

- 1: **for** $n = 1$ **to** N_{MH} **do**
- 2: Choose a site $i \sim \text{Unif}\{1, \dots, L^2\}$
- 3: Propose \mathbf{s}'_i :
4: **Ising:** $s'_i = -s_i$; ϕ^4 : $s'_i \sim \mathcal{N}(s_i, \delta^2)$
- 5: Form $\mathbf{s}' = (\mathbf{s} \setminus s_i) \cup s'_i$
- 6: Compute $\log p_\theta(\mathbf{s})$, $\log p_\theta(\mathbf{s}')$
- 7: Compute $\log p_{\text{Boltz}}(\mathbf{s}) = -\beta H(\mathbf{s})$, $\log p_{\text{Boltz}}(\mathbf{s}') = -\beta H(\mathbf{s}')$
- 8: $\log \pi(\mathbf{s}) = \log p_\theta(\mathbf{s}) + \log p_{\text{Boltz}}(\mathbf{s})$
- 9: $\log \pi(\mathbf{s}') = \log p_\theta(\mathbf{s}') + \log p_{\text{Boltz}}(\mathbf{s}')$
- 10: $\log r = \log \pi(\mathbf{s}') - \log \pi(\mathbf{s})$
- 11: $\log \alpha = \min(0, \log r)$; accept if $u < e^{\log \alpha}$ with $u \sim \text{Unif}(0, 1)$
- 12: **if** $u < e^{\log \alpha}$ **then**
- 13: $\mathbf{s} \leftarrow \mathbf{s}'$
- 14: **end if**
- 15: **end for**
- 16: **return** \mathbf{s}

The block MH changes many lattice variables in a single step, thereby reducing the number of MH iterations. In this scheme, a contiguous block B of lattice sites—for example, a 3×3 plaquette—is selected, and all variables inside the block are updated simultaneously. The proposed configuration is generated by sampling the new block values from the conditional distribution of the autoregressive model. . The acceptance probability is then evaluated using the transition amplitude as in the single-site case. A schematic description is given in Algorithm 2. In practice, we work with rectangular (geometric) blocks, and the log-density difference current and proposed configuration is approximated by summing the site-wise conditional log-probabilities over the updated block.

Algorithm 2 Block Metropolis–Hastings correction

Require: VAN-generated configuration \mathbf{s} , block size $b \times b$, number of block steps N_{block}

- 1: **for** $n = 1$ **to** N_{block} **do**
- 2: Choose block anchor (x_0, y_0) uniformly
- 3: Define $B = \{(x, y) : x \in [x_0, x_0+b-1], y \in [y_0, y_0+b-1]\}$ (periodic)
- 4: Resample $\mathbf{s}'_B \sim p_\theta(\cdot | \mathbf{s}_{\bar{B}})$ and set $\mathbf{s}' = (\mathbf{s}_{\bar{B}}, \mathbf{s}'_B)$
- 5: $\Delta \log p_\theta \approx \sum_{i \in B} [\log p_\theta(s'_i | s'_{<i}) - \log p_\theta(s_i | s_{<i})]$
- 6: $\Delta H = H(\mathbf{s}') - H(\mathbf{s})$
- 7: $\log r = \Delta \log p_\theta - \beta \Delta H$
- 8: $\log \alpha = \min(0, \log r)$; accept if $u < e^{\log \alpha}$ with $u \sim \text{Unif}(0, 1)$
- 9: **if** $u < e^{\log \alpha}$ **then**
- 10: $\mathbf{s} \leftarrow \mathbf{s}'$
- 11: **end if**
- 12: **end for**
- 13: **return** \mathbf{s}

2.5 Training and benchmark methods

The network is trained by minimizing the variational free energy

$$F_\theta = \mathbb{E}_{\mathbf{s} \sim p_\theta} \left[H(\mathbf{s}) + \frac{1}{\beta} \log p_\theta(\mathbf{s}) \right]. \quad (2.10)$$

Since the expectation is taken over samples drawn from p_θ , we use the REINFORCE gradient estimator [20]:

$$\nabla_\theta F_\theta = \mathbb{E}_{\mathbf{s} \sim p_\theta} \left[\left(H(\mathbf{s}) + \frac{1}{\beta} \log p_\theta(\mathbf{s}) - b \right) \nabla_\theta \log p_\theta(\mathbf{s}) \right], \quad (2.11)$$

where $b = \langle H + \frac{1}{\beta} \log p_\theta \rangle$ serves as a baseline to reduce variance. With a suitable choice of baseline, one can retain the physical meaning of the variational free energy while keeping the variance of the gradient estimator under control.

The training hyperparameters are as follows: learning rate $\eta = 10^{-3}$ with a ReduceLROnPlateau scheduler; batch size 500–1000; gradient clipping with norm 1.0; Adam optimizer [21] with $\beta_1 = 0.9$ and $\beta_2 = 0.999$; training epoch 50000. We employ mixed-precision training (AMP) for GPU acceleration. Details of the training procedure are given in Appendix B.

To validate sampling accuracy, we generate reference data using the following benchmark methods: for the Ising model, a GPU-accelerated Metropolis Monte Carlo with checkerboard decomposition and parallel updates; for the ϕ^4 theory, a GPU-accelerated hybrid Monte Carlo (HMC) with leapfrog integrator [22]. Both methods provide unbiased sampling of the Boltzmann distribution and are used to compute reference values of physical observables.

3 Discrete system: Ising model results

3.1 Thermodynamic observables

Figure 3 presents thermodynamic observables for the two-dimensional Ising model on a 6×6 lattice, comparing the performance of the variational autoregressive network (VAN) with and without MH corrections against exact HMC benchmarks. Panel 3a shows the magnetization as a function of the inverse temperature β . While the VAN-only results (red circles) exhibit noticeable deviations from the MC reference (black squares) in the ordered phase and near the critical region, both MH-corrected variants—single-site (green diamonds) and block with 3×3 block size update (purple stars)—agree with the reference within statistical uncertainties over the entire temperature range. This demonstrates that the MH step effectively removes the systematic bias of the pure VAN.

Panel 3b displays the corresponding magnetic susceptibility. The peak near ≈ 0.44 , which signals the phase transition. Again, the VAN-only curve slightly underestimates the peak height, whereas the two MH-corrected curves follow the MC benchmark closely.

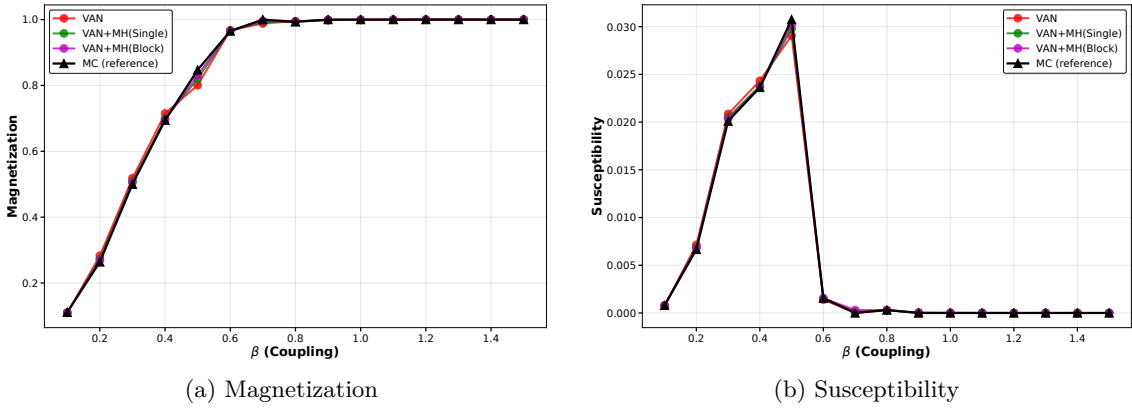


Figure 3: Thermodynamic observables for the Ising model ($L = 6$). (a):Magnetization;(b):Susceptibility. Comparison between VAN (red circles), VAN+MH (green circles), and MC benchmarks (black triangles).

3.2 Effective sample size analysis

The effective sample size (ESS) quantifies the sampling efficiency of VAN models. Figure 4 shows the ESS as a function of inverse temperature β for the Ising model. ESS remains uniformly high (close to 1) across all temperatures, indicating efficient sampling. Notably, the ESS curves with and without transfer learning overlap, indicating that transfer learning does not significantly affect sampling efficiency in this case.

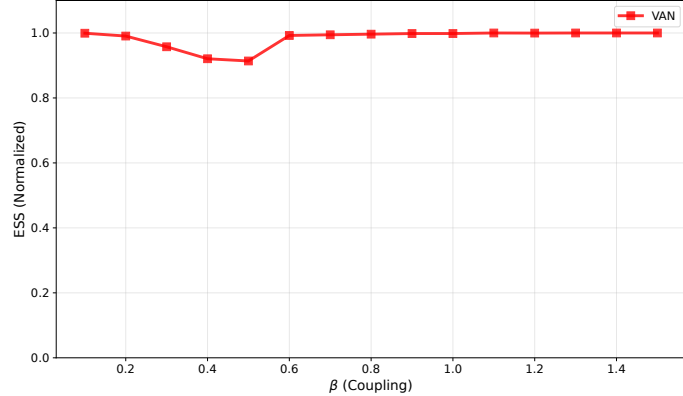


Figure 4: Effective sample size (ESS) as a function of inverse temperature β for the Ising model ($L = 6$). ESS remains uniformly high across all temperatures, indicating efficient sampling. Results with and without transfer learning overlap, indicating that transfer learning does not significantly affect ESS.

4 Continuous system: ϕ^4 theory results

Figure 5 presents a comparative analysis of the magnetization, Susceptibility and Binder cumulant for 2D ϕ^4 theory on a $L = 6$ lattice, evalutaing the performance of VAN with

an without MH corrections against HMC benchmarks. Panel 5a shows the absolute magnetization $|M|$ as a function of κ . While the results from pure VAN sampling (blue curve) exhibit a systematic negative bias relative to the HMC baseline (black curve) near critical region, both VAN with MH correction—single-MH (orange) and block MH (light blue)—closely align with the benchmark, successfully correcting this deviation.

The susceptibility χ displayed in panel 5b, and the one calculated from pure VAN sampling is noticeably suppressed in both height and sharpness compared to the HMC result. In contrast, the curves obtained after applying either single-site or block MH corrections accurately reproduce the amplitude and shape of the HMC peak. This precise overlap demonstrates that the MH step effectively restores the enhanced long-range correlations characteristic of the critical point.

Finally, panel (c) depicts the Binder cumulant U_L a scale-invariant quantity sensitive to the higher moments of the order parameter distribution. The VAN+MH results successfully replicate the non-monotonic crossing behavior of the HMC benchmark. The agreement in both the crossing point and the asymptotic values confirms that the combined autoregressive-MH scheme not only yields accurate expectation values but also correctly captures the higher-order statistics that characterize the critical universality class.

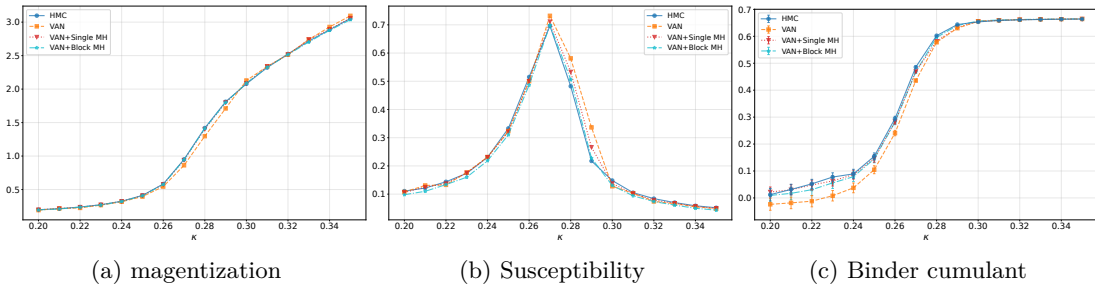
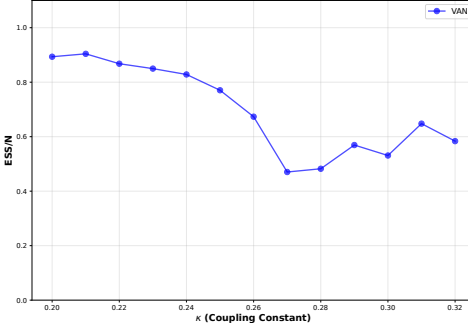


Figure 5: Thermodynamic observables of the ϕ^4 theory ($L = 6$). Blue: pure VAN sampling; orange: VAN with single-site MH; black: HMC benchmarks.

In Figure 6, the blue curve shows that ESS decreases gradually from approximately 0.82 at $\kappa = 0.20$ to near 0.47 at $\kappa = 0.27$, then slightly increases to about 0.56 at $\kappa = 0.32$. The absence of a drop near the critical coupling motivates the introduction of Metropolis-Hastings corrections to recover a high effective sample size.



(a) ESS analysis

Figure 6: Effective sample size (ESS) of the ϕ^4 theory ($L = 6$) as a function of κ .

5 Transfer learning

5.1 Transfer learning strategies

As a methodological strategy for improving training and sampling efficiency, we employ transfer learning, which allows knowledge acquired by a model in one setting to be reused in related tasks. Within the context of lattice field theory, we investigate two primary transfer scenarios: across coupling parameters and across lattice sizes.

For the ϕ^4 theory, the following two transfer protocols are studied:

- **Transfer across couplings at fixed lattice size ($L = 6$):** A base model is first trained at $\kappa = 0.20$, a value near the critical point. This model is subsequently fine-tuned at other values of κ within the range $[0.20, 0.30]$. This protocol assesses how effectively a single base model can generalize across different regions of the phase diagram.
- **Transfer across lattice sizes at fixed coupling ($\kappa = 0.27$):** A base model is trained on a lattice of size $L = 6$. Its learned representations are then transferred to larger lattices ($L = 7 - 12$) by spatially interpolating its convolutional kernels, followed by fine-tuning. This examines whether local correlation structures learned on a smaller system can facilitate learning on larger ones.

5.2 Transfer across coupling parameters

Figure 7 shows the speedup of transfer learning relative to training from scratch. We define the speedup factor as the ratio of the number of training epochs required for convergence without transfer to that with transfer. Within the explored κ range, transfer learning typically yields a speedup of about 2–3, with slightly larger gains for κ values not too far from the base point.

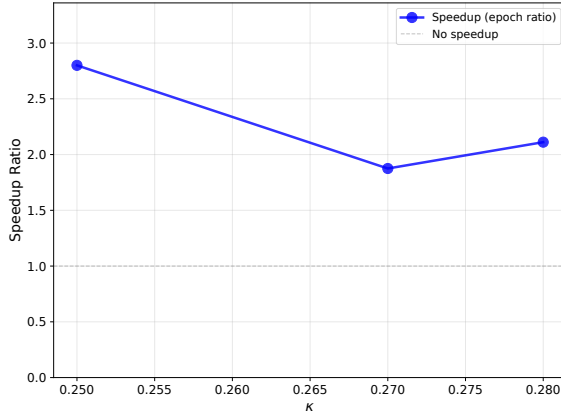


Figure 7: Training speedup from transfer learning across coupling parameters at $L = 6$ spanning κ range.

Panel 8a displays the absolute magnetization $|M|$. The VAN results quantitatively match the HMC benchmark across the entire κ range. VAN data smoothly tracks the HMC values in both the disordered and ordered phases. The close agreement indicates that the VAN correctly captures the global alignment of the field.

The susceptibility χ , is shown in panel 8b. The VAN accurately reproduces the sharp peak in χ , including its amplitude and the shape of its wings. The precise overlap of the VAN and HMC peaks demonstrates that VAN faithfully captures the enhanced long-range fluctuations at the phase transition, with no sign of artificial suppression or broadening of the critical region.

Panel 8c presents the Binder cumulant U . The VAN curve successfully reproduces the non-monotonic crossing behavior of the HMC benchmark: U approaches zero from below in the disordered phase, exhibits a rapid rise through κ_c , and saturates at a positive value in the ordered phase.

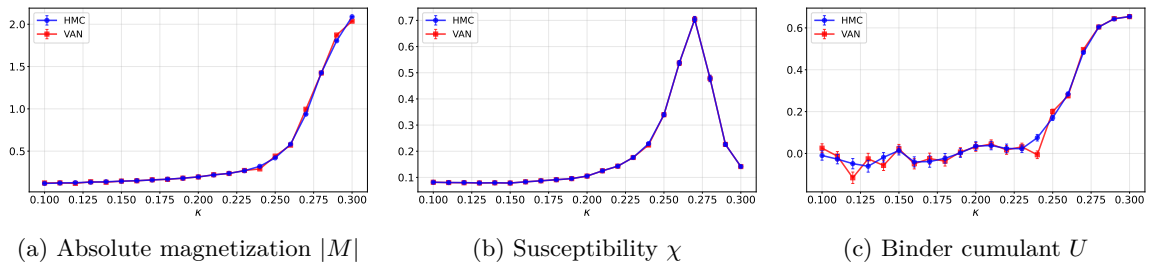


Figure 8: Observables at $L = 6$ as functions of κ . Comparison between VAN (red squares) and HMC benchmarks (blue circles). The critical point $\kappa_c \approx 0.27$ is indicated by the vertical dashed line. **(a)** The absolute magnetization; **(b)** The susceptibility; **(c)** The Binder cumulant.

5.3 Transfer across lattice sizes

Figure 9 quantifies the computational speedup achieved through transfer learning across lattice sizes. When a model pre-trained at $L = 6$ is fine-tuned for larger systems ($L = 7, 8, 9$), the observed speedup factors range from 1.5 to 2.5. This improvement, while more modest than that obtained for coupling-parameter transfer, still corresponds to a significant reduction in the required training time.

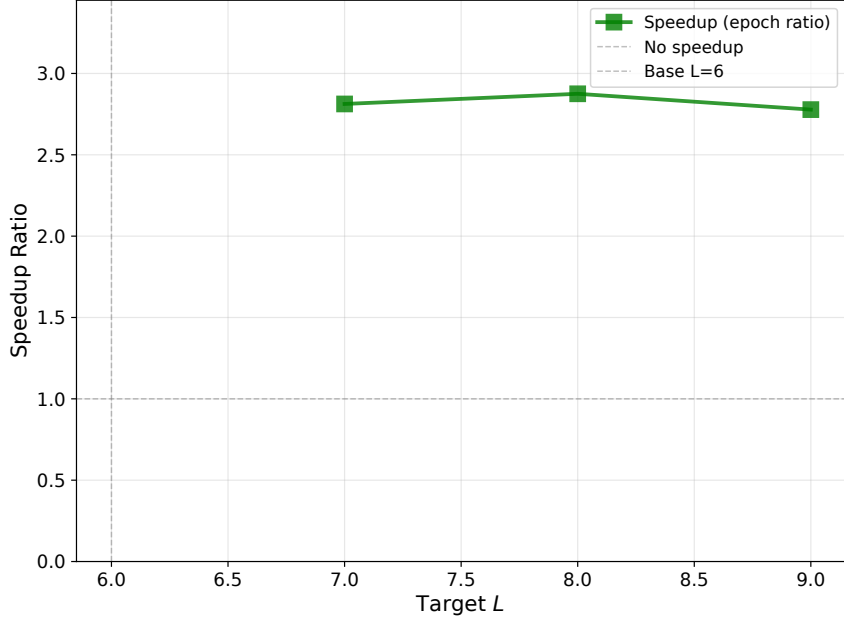


Figure 9: Training speedup from lattice-size transfer learning at fixed $\kappa = 0.27$ to the target lattice size L .

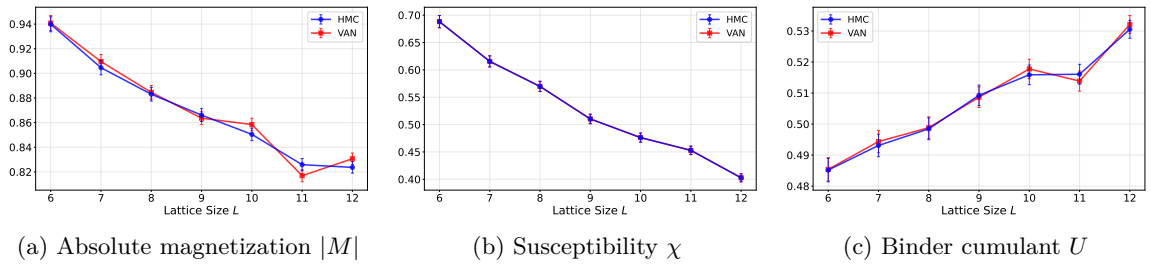


Figure 10: Observables at fixed $\kappa = 0.27$ as functions of lattice size L ($L = 6-12$). Comparison between VAN (red squares) and HMC benchmarks (blue circles). **(a)** Absolute magnetization $|M|$; **(b)** susceptibility χ ; **(c)** Binder cumulant U .

Figure 10 shows key observables for the ϕ^4 theory at fixed coupling $\kappa = 0.27$, computed across lattice sizes $L = 6 - 12$ using a variational autoregressive network (VAN) pretrained on $L = 6$ and subsequently transferred to larger systems via spatial kernel interpolation

and fine-tuning. The VAN results (red squares) are compared with hybrid Monte Carlo (HMC) benchmarks (blue circles). All three panels illustrate that the transferred model faithfully reproduces the HMC references within statistical uncertainties, confirming that the locally learned correlation patterns can be successfully extended to larger lattices without substantial loss of accuracy.

Together with the speed-up factors reported in Figure 9 (typically $23\times$ for coupling-parameter transfer and $1.52.5\times$ for size transfer), these results demonstrate that transfer learning not only preserves physical accuracy across different lattice sizes, but also substantially reduces the computational cost of training larger-scale autoregressive samplers.

5.4 KL divergence and training complexity

To elucidate the origin of the training speedup achieved via transfer learning, we analyze the correlation between the complexity of the target distribution and the number of epochs required for convergence. The complexity is quantified by the Kullback-Leibler (KL) divergence between the normalized empirical magnetization distribution obtained from HMC, P , and a standard Gaussian reference,

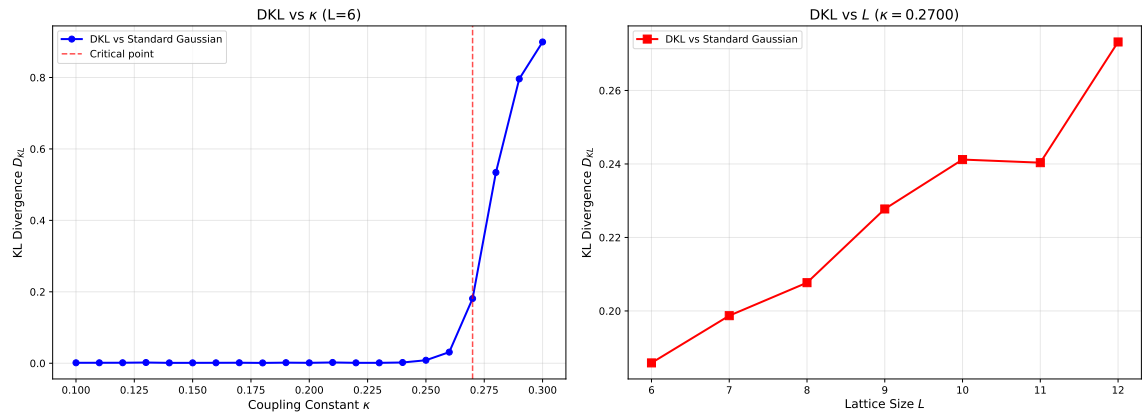


Figure 11: KL divergence D_{KL} as a function of κ and L . Left: D_{KL} versus κ at fixed $L = 6$. In the low- κ (disordered) region, D_{KL} is close to 0, indicating that the magnetization distribution is nearly Gaussian; it increases near the critical point ($\kappa \approx 0.27$) and becomes large in the high- κ (ordered) region due to the emergence of a bimodal structure. Right: D_{KL} versus lattice size L at fixed $\kappa = 0.27$.

$$D_{KL}(P||Q) = \int p(x) \log \frac{p(x)}{q(x)} dx. \quad (5.1)$$

A larger D_{KL} indicates a greater deviation from a simple unimodal Gaussian shape, corresponding to a more structured and hence more "complex" distribution for the model to learn.

Figure 11 plots this divergence as a function of the hopping parameter κ and the lattice size L . For a fixed $L = 6$ (left panel), D_{KL} is minimal in the deep disordered phase (small κ)

and grows as the system approaches the critical region, peaking in the ordered phase where the magnetization distribution becomes distinctly bimodal. This non-monotonic variation with κ aligns with the progression from a simple paramagnet to a system with spontaneous symmetry breaking. For a fixed $\kappa = 0.27$ (right panel), D_{KL} increases moderately with L , reflecting the gradual enhancement of long-range correlations and the sharpening of finite-size effects on larger lattices. The monotonic growth of distributional complexity with system size provides a quantitative basis for understanding the scaling of training difficulty.

Figure 12 shows a nearly linear relationship between the KL divergence and the number of epochs needed for training to converge: a larger D_{KL} —corresponding to a more complex, non-Gaussian magnetization distribution—consistently requires more training time. This scaling explains the efficiency of transfer learning. When a model is transferred from a source point with high distributional complexity to a nearby target, the network already possesses a good approximation of the dominant short- and medium-range correlations. Fine-tuning therefore primarily adjusts the parameters that govern longer-range fluctuations, substantially reducing the number of epochs compared to training from scratch.

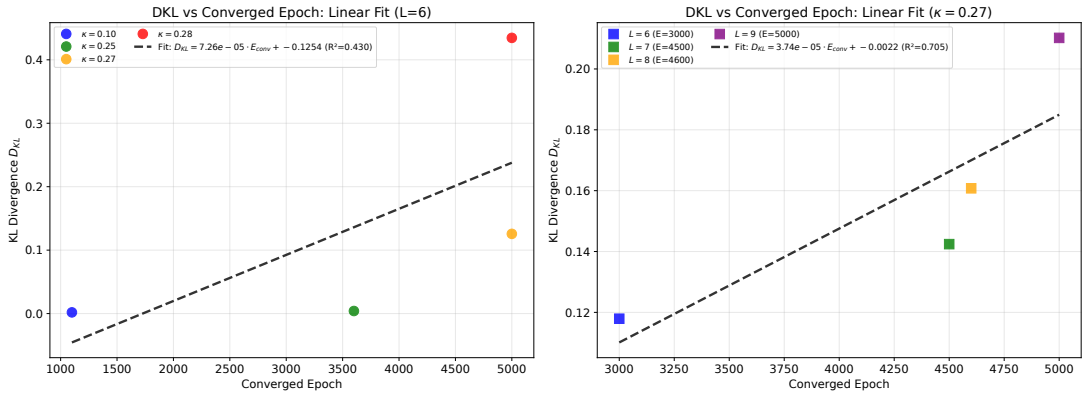


Figure 12: Linear fits between the number of training epochs to convergence and KL divergence. Left: relation between epochs and D_{KL} at different κ values for fixed $L = 6$. Right: relation between epochs and D_{KL} at different lattice sizes L for fixed $\kappa = 0.27$. Dashed lines show linear fits; fit formulas and R^2 values are indicated in the panels.

Figure 13 traces the evolution of the KL divergence and the magnetization error throughout the training process, providing direct support for the preceding analysis. The plots show that, when fine-tuning from a pretrained base model, both D_{KL} and the observable errors drop more rapidly and reach convergence in substantially fewer epochs compared to training from scratch. This acceleration is particularly pronounced for target parameter values close to the base point, where the underlying distributional structure—and therefore the required parameter adjustments—are most similar.

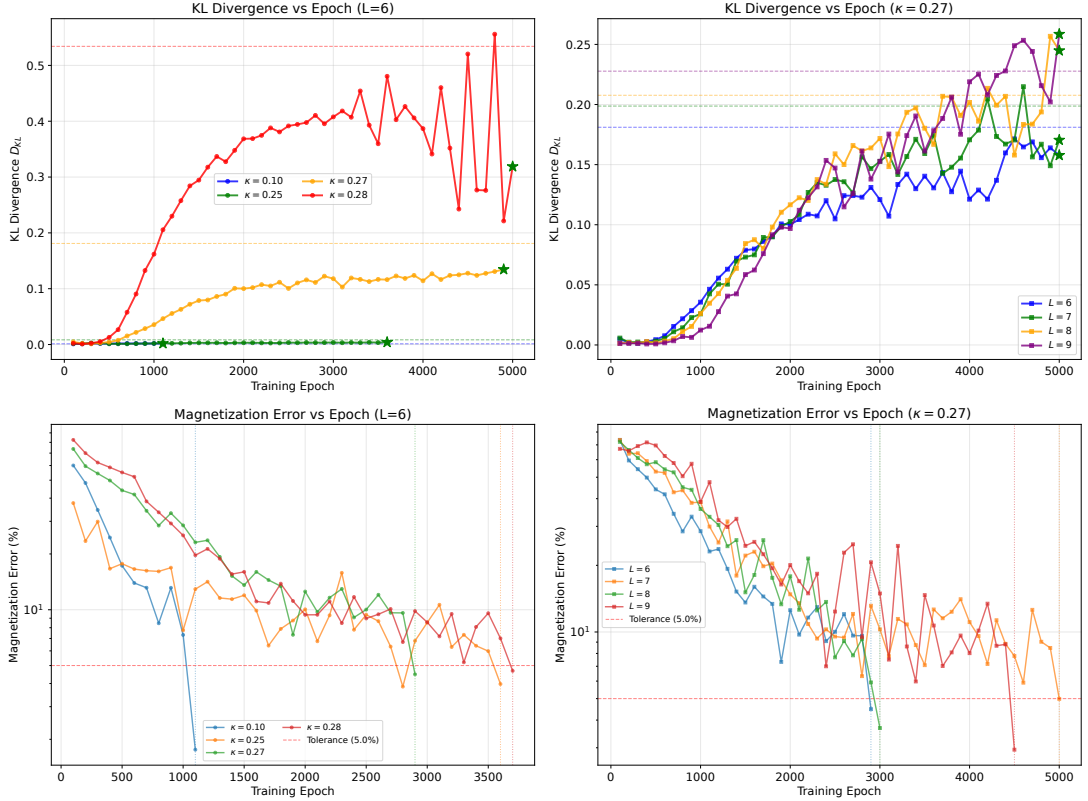


Figure 13: Comprehensive analysis of the training process. Top left: D_{KL} versus training epochs at different κ values for fixed $L = 6$. Top right: D_{KL} versus training epochs at different L values for fixed $\kappa = 0.27$. Bottom left: magnetization error versus training epochs at different κ values for fixed $L = 6$. Bottom right: magnetization error versus training epochs at different L values for fixed $\kappa = 0.27$. Green stars mark convergence points; dashed lines show HMC reference values or tolerance thresholds.

In summary, the efficiency of transfer learning stems from the hierarchical representation learned by the network. The shallow (early) convolutional layers predominantly capture short-range correlation patterns, which are largely universal across nearby points in parameter space and can therefore be reused directly. In contrast, the deeper layers encode longer-range, system-specific features that must be adapted to the target distribution via fine-tuning. The observed near-linear scaling between the KL divergence—a measure of distributional complexity—and the required training epochs provides a quantitative foundation for predicting the computational cost of training and for rationally designing transfer strategies.

6 Conclusion

In this work, we have extended variational autoregressive networks (VANs) from spin systems to continuous ϕ^4 scalar field theory, systematically investigating both Metropolis–Hastings (MH) correction strategies and transfer-learning schemes. On the methodological

front, we established a conceptual correspondence between autoregressive sampling and traditional Monte Carlo approaches: site-by-site conditional sampling parallels Metropolis single-site updates, while block-wise resampling resembles non-local cluster updates. Building on this analogy, we introduced single-site and block MH corrections applied to VAN-generated proposals. For the ϕ^4 theory, the normalized effective sample size (ESS) remains near unity (≈ 0.8) for single-site MH corrections and stays within a practical range for 3×3 block updates, confirming that the learned distributions already closely approximate the auxiliary target density.

We further examined transfer learning across coupling parameters and lattice sizes. Transfer along the coupling axis (κ) yields training speed-up factors of roughly 2–3, whereas extending from $L = 6$ to $L = 9$ at fixed κ provides speed-ups of about 1.5–2.5. By analyzing the relationship between KL divergence—a measure of distributional complexity—and the number of epochs required for convergence, we observed an approximately linear positive correlation, which quantitatively explains the efficiency gains achieved through transfer learning.

Numerical experiments demonstrate that the VAN+MH framework produces results fully consistent with hybrid Monte Carlo (HMC) benchmarks for both the Ising model and the ϕ^4 theory. Within the studied parameter ranges, no pronounced critical slowing-down is observed near the critical point, supporting the viability of autoregressive sampling as an efficient tool for lattice field simulations. Promising future directions include extending the approach to gauge theories, investigating finite-size scaling at larger lattice volumes, and combining VAN proposals with other correction mechanisms—such as Langevin-type updates or reweighting techniques inspired by normalizing flows.

7 Acknowledgments

The authors would like to thank Gert Art, Jianhui Zhang and Kai Zhou for some useful discussion. We also thank the the Southern Nuclear Science Computing Center(SNSC) for providing computing resources. SYC is supported by the China Scholarship Council (No. 202308420042) and a Swansea University joint PhD project.

References

- [1] S. Schaefer, R. Sommer and F. Virotta, *Critical slowing down and error analysis in lattice qcd simulations*, *Nucl. Phys. B* **845** (2011) 93 [[1009.5228](#)].
- [2] M. Lüscher, *Properties and uses of the wilson flow in lattice qcd*, *JHEP* **08** (2010) 071 [[1006.4518](#)].
- [3] D.J. Rezende and S. Mohamed, *Variational inference with normalizing flows*, *Proceedings of the 32nd International Conference on Machine Learning* **37** (2015) 1530 [[1505.05770](#)].
- [4] L. Dinh, J. Sohl-Dickstein and S. Bengio, *Density estimation using real-nvp*, *International Conference on Learning Representations* (2017) [[1605.08803](#)].
- [5] R.T.Q. Chen, Y. Rubanova, J. Bettencourt and D. Duvenaud, *Neural ordinary differential equations*, *Advances in Neural Information Processing Systems* **31** (2018) [[1806.07366](#)].

- [6] K.A. Nicoli, C.J. Anders, L. Funcke, T. Hartung, K. Jansen, P. Kessel et al., *Estimation of thermodynamic observables in lattice field theories with deep generative models*, *Phys. Rev. Lett.* **126** (2021) 032001 [[2007.07115](#)].
- [7] J. Ho, A. Jain and P. Abbeel, *Denoising diffusion probabilistic models*, *Advances in Neural Information Processing Systems* **33** (2020) 6840 [[2006.11239](#)].
- [8] Y. Song, J. Sohl-Dickstein, D.P. Kingma, A. Kumar, S. Ermon and B. Poole, *Score-based generative modeling through stochastic differential equations*, *International Conference on Learning Representations* (2021) [[2011.13456](#)].
- [9] Y. Lipman, R.T.Q. Chen, H. Ben-Hamu, M. Nickel and M. Le, *Flow matching for generative modeling*, *International Conference on Learning Representations* (2023) [[2210.02747](#)].
- [10] X. Liu, C. Gong and Q. Liu, *Flow straight and fast: Learning to generate and transfer data with rectified flow*, *International Conference on Learning Representations* (2023) [[2209.03003](#)].
- [11] M.S. Albergo, G. Kanwar and P.E. Shanahan, *Flow-based generative models for markov chain monte carlo in lattice field theory*, *Phys. Rev. D* **100** (2019) 034515 [[1904.12072](#)].
- [12] K.A. Nicoli, C.J. Anders, L. Funcke, T. Hartmann, K. Jansen, P. Kessel et al., *Asymptotically unbiased estimation of physical observables with neural samplers*, *Phys. Rev. E* **101** (2020) 023304 [[1910.13496](#)].
- [13] R. Abbott, M.S. Albergo, A. Botev, D. Boyda, K. Cranmer, D.C. Hackett et al., *Aspects of scaling and scalability for flow-based sampling of lattice qcd*, *arXiv preprint* (2022) [[2211.07541](#)].
- [14] G. Kanwar, M.S. Albergo, D. Boyda, K. Cranmer, D.C. Hackett, S. Racanière et al., *Equivariant flow-based sampling for lattice gauge theory*, *Phys. Rev. Lett.* **125** (2020) 121601 [[2003.06413](#)].
- [15] A. van den Oord, N. Kalchbrenner and K. Kavukcuoglu, *Pixel recurrent neural networks*, *Proceedings of the 33rd International Conference on Machine Learning* **48** (2016) 1747 [[1601.06759](#)].
- [16] M. Germain, K. Gregor, I. Murray and H. Larochelle, *Made: Masked autoencoder for distribution estimation*, *Proceedings of the 32nd International Conference on Machine Learning* **37** (2015) 881 [[1502.03509](#)].
- [17] D. Wu, L. Wang and P. Zhang, *Solving statistical mechanics using variational autoregressive networks*, *Phys. Rev. Lett.* **122** (2019) 080602 [[1902.04942](#)].
- [18] L. Wang, Y. Jiang, L. He and K. Zhou, *Continuous-mixture autoregressive networks for efficient variational calculation of many-body systems*, [2005.04857](#).
- [19] N. Metropolis, A.W. Rosenbluth, M.N. Rosenbluth, A.H. Teller and E. Teller, *Equation of state calculations by fast computing machines*, *J. Chem. Phys.* **21** (1953) 1087.
- [20] S. Mohamed, M. Rosca, M. Figurnov and A. Mnih, *Monte carlo gradient estimation in machine learning*, *J. Mach. Learn. Res.* **21** (2020) 1 [[1906.10652](#)].
- [21] D.P. Kingma and J. Ba, *Adam: A method for stochastic optimization*, *International Conference on Learning Representations* (2015) [[1412.6980](#)].
- [22] S. Duane, A.D. Kennedy, B.J. Pendleton and D. Roweth, *Hybrid monte carlo*, *Phys. Lett. B* **195** (1987) 216.

- [23] U. Wolff, *Collective monte carlo updating for spin systems*, *Phys. Rev. Lett.* **62** (1989) 361.
- [24] U. Wolff, *Critical slowing down*, *Nucl. Phys. B Proc. Suppl.* **17** (1990) 93.
- [25] G. Parisi and Y.S. Wu, *Perturbation theory without gauge fixing*, *Scientia Sinica* **24** (1981) 483.
- [26] P.H. Damgaard and H. Hüffel, *Stochastic quantization*, *Phys. Rep.* **152** (1987) 227.
- [27] G.O. Roberts and R.L. Tweedie, *Exponential convergence of langevin distributions and their discrete approximations*, *Bernoulli* **2** (1996) 341.
- [28] L. Wang, G. Aarts and K. Zhou, *Diffusion models as stochastic quantization in lattice field theory*, *JHEP* **05** (2024) 060 [[2309.17082](https://arxiv.org/abs/2309.17082)].

A Network architecture

PixelCNN autoregressive architecture (Ising and ϕ^4). For both the discrete Ising model and the continuous two-dimensional ϕ^4 theory, we adopt the same masked-convolution PixelCNN backbone to realize an autoregressive factorization. The network input is a batch of configuration tensors with shape $[B, 1, L, L]$, and a raster-scan (row-major) ordering is enforced by causal masks. Concretely, the first layer is a masked convolution with `exclusive=True`, corresponding to an *A-mask* that removes information from the current site and all future sites. This is followed by N masked convolution layers with `exclusive=False`, corresponding to *B-masks* that allow the current site while still excluding future sites. Between masked convolutions we use PReLU nonlinearities; optionally, we employ residual blocks of the form 1×1 convolution \rightarrow PReLU \rightarrow masked convolution, added back to the input. The kernel size is set by `half_kernel_size` (e.g. `half_kernel_size=3` gives a 7×7 kernel), while `net_width` (e.g. 64/128) and `net_depth` (e.g. 3–6) control the channel width and depth, respectively.

difference between Ising and ϕ^4 heads. The only essential difference lies in the output head and the resulting conditional distribution. For the Ising model, the network outputs a single channel followed by a Sigmoid activation, yielding Bernoulli probabilities $p_\theta(\sigma_{ij} = +1 \mid \sigma_{<ij}) \in (0, 1)$; sampling is performed via `torch.bernoulli(p)` and mapped to spins by $2\text{Bernoulli}(p) - 1 \in \{-1, +1\}$, with an optional global Z_2 flip augmentation. For the ϕ^4 theory, the network outputs two channels interpreted as $(\mu, \log \sigma)$, parameterizing a Gaussian conditional $p_\theta(\phi_{ij} \mid \phi_{<ij}) = \mathcal{N}(\mu_{ij}, \sigma_{ij}^2)$; no Sigmoid is applied, and $\log \sigma$ is clamped for numerical stability before sampling each site sequentially from the corresponding Normal distribution.

B Training algorithms

Algorithm 3 Training variational autoregressive networks (VAN)

Require: Model M_θ , config \mathcal{C} , epochs N_{epoch} , batch size B , inverse temperature β

Ensure: Trained model M_{θ^*}

- 1: $\text{opt} \leftarrow \text{Adam}(M_\theta; \eta=10^{-3}, \beta_1=0.9, \beta_2=0.999)$; $\text{sched} \leftarrow \text{ReduceLROnPlateau}(\text{opt})$
- 2: **for** $e = 1$ **to** N_{epoch} **do**
- 3: $\{(\mathbf{s}^{(i)}, \log p_\theta(\mathbf{s}^{(i)}))\}_{i=1}^B \sim M_\theta$; $E^{(i)} \leftarrow H(\mathbf{s}^{(i)}; \mathcal{C})$
- 4: $F^{(i)} \leftarrow E^{(i)} + \beta^{-1} \log p_\theta(\mathbf{s}^{(i)})$; $b \leftarrow \frac{1}{B} \sum_i F^{(i)}$; $A^{(i)} \leftarrow F^{(i)} - b$
- 5: $\mathcal{L} \leftarrow \frac{1}{B} \sum_i A^{(i)} \log p_\theta(\mathbf{s}^{(i)})$
- 6: $\text{opt.zero_grad}()$; $\mathcal{L}.\text{backward}()$; $\text{clip_grad_norm}(\theta, 1.0)$; $\text{opt.step}()$; $\text{sched.step}(\mathcal{L})$
- 7: **end for**
- 8: **return** M_{θ^*}

Algorithm 4 Transfer learning algorithm

Require: Base model M_{θ_0} , target parameters $\mathcal{C}_{\text{target}}$, number of fine-tuning steps N_{fine} , batch size B

Ensure: Fine-tuned model M_{θ^*}

- 1: Load base model: $M_\theta \leftarrow \text{LoadModel}(M_{\theta_0})$
- 2: **Optional:** freeze early-layer parameters
- 3: **for** each early layer $\ell \in M_\theta.\text{early_layers}$ **do**
- 4: $\ell.\text{requires_grad} \leftarrow \text{False}$
- 5: **end for**
- 6: Initialize optimizer with smaller learning rate: $\text{opt} \leftarrow \text{Adam}(M_\theta, \eta = 10^{-4})$
- 7: **for** $t = 1$ **to** N_{fine} **do**
- 8: Sample a batch of configurations: $\{\mathbf{s}^{(i)}, \log p_\theta(\mathbf{s}^{(i)})\}_{i=1}^B \sim M_\theta$
- 9: Compute energies at target parameters: $E^{(i)} \leftarrow H(\mathbf{s}^{(i)}, \mathcal{C}_{\text{target}}) \quad \forall i$
- 10: Compute variational free energy estimates: $F^{(i)} \leftarrow E^{(i)} + \frac{1}{\beta} \log p_\theta(\mathbf{s}^{(i)})$
- 11: Compute baseline: $b \leftarrow \frac{1}{B} \sum_{i=1}^B F^{(i)}$
- 12: Compute advantages: $A^{(i)} \leftarrow F^{(i)} - b \quad \forall i \in [1, B]$
- 13: Compute REINFORCE loss: $\mathcal{L} \leftarrow \frac{1}{B} \sum_{i=1}^B A^{(i)} \cdot \log p_\theta(\mathbf{s}^{(i)})$
- 14: Zero gradients: $\text{opt.zero_grad}()$
- 15: Backpropagate: $\mathcal{L}.\text{backward}()$
- 16: Clip gradients: $\text{clip_grad_norm}(\theta, \text{max_norm} = 1.0)$
- 17: Update parameters: $\text{opt.step}()$
- 18: **end for**
- 19: **return** M_{θ^*}

C Detailed comparison between generative models and MC algorithms

This appendix provides a brief, self-contained discussion of the methodological connections between representative generative models and traditional Monte Carlo algorithms.

C.1 Overview table

Table 1 summarizes the correspondence between update schemes, typical correction strategies, and computational bottlenecks.

Table 1: Comparison of generative models and traditional MC algorithms.

Algorithm type	Update scheme	MC analogue	Correction strategy	Main bottleneck
Autoregressive (AR)	Site-wise	Single-site Metropolis	Single-site / block MH	Computing p_θ
Block-update AR	Block parallel	Cluster-like non-local moves	Block MH	Multiple evaluations of p_θ
Diffusion models (DM)	Global denoising	Langevin dynamics	MALA / importance reweighting	Gradient ∇H
Stochastic Path sampler (SPS)	Global in fictitious time	Langevin dynamics	MALA / implicit	Action gradients
Normalizing flows (NF)	Global transforms	–	MH / reweighting	Jacobian determinant
Flow matching (FM)	Global flow	–	MH / importance reweighting	Integrating velocity fields
Traditional Metropolis	Single-site random	–	Inherently exact (up to discretization)	Slow mixing near criticality
Wolff algorithm	Cluster flips	–	Inherently exact	Cluster identification
HMC	Global symplectic	–	Inherently exact	Gradient ∇H
Langevin dynamics	Global update	–	Exact	Long fictitious-time evolution

C.2 Block updates

The Wolff algorithm [23] achieves non-local updates by identifying correlated clusters and flipping them collectively, effectively mitigating critical slowing down [1, 24]. Our block-update strategy in the autoregressive setting is conceptually inspired by this idea: by updating geometric blocks or chosen sets of sites simultaneously, we can perform larger moves in configuration space at each MH step. However, unlike the Wolff algorithm, our blocks are simple geometric regions rather than clusters constructed via specific rules; detailed balance is enforced by MH acceptance with respect to the auxiliary target $\pi(\mathbf{s})$.

C.3 Diffusion models, Langevin dynamics, and stochastic quantization

Diffusion models implement a Markov chain that gradually transforms noise into data through a sequence of denoising steps [7, 8]. In continuous time, they can be viewed as simulating a stochastic differential equation (SDE)

$$d\phi = f_\theta(\phi, t)dt + g(t)dW_t, \quad (\text{C.1})$$

where W_t is a Wiener process and f_θ is related to a score function. Discrete-time implementations resemble Langevin updates with a learned drift term.

In lattice field theory, stochastic quantization [25, 26] introduces a fictitious time τ through a Langevin equation

$$\frac{\partial \phi_x(\tau)}{\partial \tau} = -\frac{\delta S[\phi]}{\delta \phi_x} + \eta_x(\tau), \quad \langle \eta_x(\tau) \eta_y(\tau') \rangle = 2\delta_{xy}\delta(\tau - \tau'), \quad (\text{C.2})$$

whose stationary distribution is the desired Boltzmann distribution. Discretizing this evolution in τ yields algorithms that are formally exact in the continuum limit but suffer from discretization errors at finite step size. To eliminate these errors, one can use Metropolis-adjusted Langevin algorithms (MALA) [27], where each Langevin proposal is accepted or rejected according to the MH criterion.

Neural stochastic quantization methods [28] approximate the drift term with neural networks, combining the physical structure of Langevin dynamics with the expressive power

of learned models. Conceptually, this is complementary to autoregressive approaches: the former focuses on continuous-time evolution of fields, while the latter focuses on factorization and direct autoregressive sampling.

C.4 Normalizing flows and flow matching

Normalizing flows (NF) construct an invertible mapping $f_\theta : \mathbb{R}^{L^2} \rightarrow \mathbb{R}^{L^2}$ that transforms a simple base distribution $p_0(z)$ into a flexible distribution over fields via $\phi = f_\theta(z)$; the resulting density is

$$p_\theta(\phi) = p_0(f_\theta^{-1}(\phi)) \left| \det \frac{\partial f_\theta^{-1}}{\partial \phi} \right|. \quad (\text{C.3})$$

Flow matching and related methods [9, 10] learn a continuous flow that interpolates between the base and target distributions. In lattice field theory, NF-based samplers have been combined with MH corrections or reweighting to ensure unbiased estimates [6, 11, 12, 14].

Compared with autoregressive models, NF and flow-based methods typically perform global updates and involve computing Jacobian determinants or solving ODEs, whereas autoregressive models rely on masked convolutions and local conditional distributions. Each approach has its own trade-offs in terms of expressivity, computational cost, and ease of combining with MH corrections.

D Analytical VAN for a two-dimensional Gaussian mixture

We briefly summarize the analytical form of a VAN for a two-dimensional Gaussian mixture, used as a toy model to illustrate the autoregressive factorization.

Consider a target distribution composed of two Gaussian components:

$$p(s_1, s_2) = \frac{1}{2} \mathcal{N}(\boldsymbol{\mu}_L, \Sigma) + \frac{1}{2} \mathcal{N}(\boldsymbol{\mu}_R, \Sigma), \quad (\text{D.1})$$

where $\boldsymbol{\mu}_L = (-\mu, -\mu)^T$ and $\boldsymbol{\mu}_R = (\mu, \mu)^T$ are the means of the left and right modes, respectively, and the covariance matrix is

$$\Sigma = \begin{pmatrix} \sigma^2 & \rho\sigma^2 \\ \rho\sigma^2 & \sigma^2 \end{pmatrix} \quad (\text{D.2})$$

with correlation coefficient $\rho \in (-1, 1)$.

The VAN factorization expresses the joint distribution as

$$p(s_1, s_2) = p(s_1) p(s_2 | s_1). \quad (\text{D.3})$$

The marginal $p(s_1)$ is obtained by integrating out s_2 :

$$p(s_1) = \frac{1}{2} \mathcal{N}(s_1; -\mu, \sigma^2) + \frac{1}{2} \mathcal{N}(s_1; \mu, \sigma^2), \quad (\text{D.4})$$

which is a bimodal distribution with peaks at $s_1 = \pm\mu$.

For a bivariate Gaussian, the conditional distribution of s_2 given s_1 is again Gaussian, with mean and variance

$$\sigma_{2|1}^2 = \sigma^2(1 - \rho^2), \quad \mu_{\text{cond}}(s_1; \mu_1, \mu_2) = \mu_2 + \rho(s_1 - \mu_1). \quad (\text{D.5})$$

Thus the conditional means of the two components are

$$\mu_L(s_1) = -\mu + \rho(s_1 + \mu), \quad (\text{D.6})$$

$$\mu_R(s_1) = \mu + \rho(s_1 - \mu), \quad (\text{D.7})$$

with a common conditional variance $\sigma_{2|1}^2$.

The posterior weight of the left component given s_1 is

$$w(s_1) = \frac{\mathcal{N}(s_1; -\mu, \sigma^2)}{\mathcal{N}(s_1; -\mu, \sigma^2) + \mathcal{N}(s_1; \mu, \sigma^2)} = \frac{1}{1 + \exp\left(\frac{2\mu s_1}{\sigma^2}\right)}, \quad (\text{D.8})$$

which is a sigmoid function of s_1 . The full conditional distribution is therefore

$$p(s_2|s_1) = w(s_1)\mathcal{N}(s_2; \mu_L(s_1), \sigma_{2|1}^2) + [1 - w(s_1)]\mathcal{N}(s_2; \mu_R(s_1), \sigma_{2|1}^2). \quad (\text{D.9})$$

The VAN sampling procedure is: first draw s_1 from the bimodal marginal $p(s_1)$, then compute the posterior weight $w(s_1)$ and draw s_2 from the conditional mixture $p(s_2|s_1)$. The posterior weight ensures that samples are correctly routed to the appropriate mode: when $s_1 < 0$, $w(s_1) > 1/2$ and the left mode is favored, whereas the right mode is favored. This mechanism explains the characteristic L-shaped trajectories observed during sampling, where samples branch into two modes depending on the value of s_1 .